

# SurgT challenge: Benchmark of Soft-Tissue Trackers for Robotic Surgery

João Cartucho<sup>a</sup>, Alistair Weld<sup>a</sup>, Samyakh Tukra<sup>a</sup>, Haozheng Xu<sup>a</sup>, Hiroki Matsuzaki<sup>b</sup>, Taiyo Ishikawa<sup>b</sup>, Minjun Kwon<sup>c</sup>, Yong Eun Jang<sup>c</sup>, Kwang-Ju Kim<sup>c</sup>, Gwang Lee<sup>d</sup>, Bizhe Bai<sup>e</sup>, Lueder Kahrs<sup>e</sup>, Lars Boecking<sup>f</sup>, Simeon Allmendinger<sup>f</sup>, Leopold Müller<sup>f</sup>, Yitong Zhang<sup>g</sup>, Yueming Jin<sup>g</sup>, Bano Sophia<sup>g</sup>, Francisco Vasconcelos<sup>g</sup>, Wolfgang Reiter<sup>h</sup>, Jonas Hajek<sup>h</sup>, Bruno Silva<sup>i,j,k</sup>, Lukas R. Buschle<sup>l</sup>, Estevão Lima<sup>i,j</sup>, João L. Vilaça<sup>k</sup>, Sandro Queirós<sup>i,j</sup>, Stamatia Giannarou<sup>a</sup>

<sup>a</sup>The Hamlyn Centre for Robotic Surgery, Imperial College London, United Kingdom

<sup>b</sup>Company Name: "Jmees", Japan

<sup>c</sup>Company Name: Electronics and Telecommunications Research Institute (ETRI), Daejeon, South Korea

<sup>d</sup>Ajou University, Gyeonggi-do, South Korea

<sup>e</sup>Medical Computer Vision and Robotics Lab, University of Toronto, Canada

<sup>f</sup>Karlsruher Institut für Technologie: (KIT), Germany

<sup>g</sup>Surgical Robot Vision, University College London, United Kingdom

<sup>h</sup>Company Name: RIWOLink GmbH, Munich, Germany

<sup>i</sup>Life and Health Sciences Research Institute (ICVS), School of Medicine, University of Minho, Braga, Portugal

<sup>j</sup>ICVS/3B's - PT Government Associate Laboratory, Braga/Guimarães, Portugal

<sup>k</sup>2Ai - School of Technology, IPCA, Barcelos, Portugal

<sup>l</sup>KARL STORZ SE & Co. KG, Tuttlingen, Germany

---

## Abstract

This paper introduces the "SurgT: Surgical Tracking" challenge which was organised in conjunction with the 25th International Conference on Medical Image Computing and Computer-Assisted Intervention (MICCAI 2022). There were two purposes for the creation of this challenge: (1) the establishment of the first standardised benchmark for the research community to assess soft-tissue trackers; and (2) to encourage the development of unsupervised deep learning methods, given the lack of annotated data in surgery. A dataset of 157 stereo endoscopic videos from 20 clinical cases, along with stereo camera calibration parameters, have been provided. The participants were tasked with the development of algorithms to track a bounding box on stereo endoscopic videos. At the end of the challenge, the developed methods were assessed on a previously hidden test subset. This assessment uses benchmarking metrics that were purposely developed for this challenge and are now available online. The teams were ranked according to their Expected Average Overlap (EAO) score, which is a weighted average of the Intersection over Union (IoU) scores. The performance evaluation study verifies the efficacy of unsupervised deep learning algorithms in tracking soft-tissue. The best-performing method achieved an EAO score of 0.583 in the test subset. The dataset and benchmarking tool created for this challenge have been made publicly available. This challenge is expected to contribute to the development of autonomous robotic surgery and other digital surgical technologies.

---

## 1. Introduction

Tracking soft-tissue is a crucial task in Computer-Assisted Interventions (CAI), with a range of applications including autonomous tissue scanning (Zhan et al., 2020; Wang et al., 2022), autonomous tissue manipula-

tion (Wang et al., 2018), and other autonomous tasks in general. Besides enabling autonomy, tracking soft-tissue also allows estimating tissue deformations from the endoscopic video (Giannarou et al., 2016), which has the added benefit of being usable for evaluating non-rigid reconstruction algorithms (Garg et al., 2013). Estimating

soft-tissue deformations is crucial for augmented reality applications, such as the overlay of tumours or blood vessels on the endoscopic video for surgical guidance (Nicolau et al., 2011; Collins et al., 2020). Medical applications require accurate trackers that are robust to the dynamic conditions of surgical scenes. Therefore, prior to being utilized in real-world practice, tissue trackers need to be evaluated on a large and diverse surgical dataset that captures multiple challenges present in surgery, such as when the tracked region is occluded by a surgical instrument. The general problem of tracking has been well studied within the computer vision community, focusing on natural scenes, e.g., VOT (Kristan et al., 2016). However, a dataset for tracking soft-tissue in surgical scenes is still lacking which halts any forward progress in this field. For the task of surgical tissue 3D reconstruction, datasets such as SCARED (Allan et al., 2021), MTL (Weld et al., 2022) and EndoSLAM (Ozyoruk et al., 2021) have been created for supporting the development and evaluation of 3D reconstruction algorithms. Similarly, publicly available datasets have been created for surgical instrument segmentation (Allan et al., 2019) or surgical workflow analysis (Bodenstedt et al., 2021), but when it comes to tracking soft-tissue, there is no publicly available dataset. To address this limitation, we propose "SurgT: Surgical Tracking", a first-of-its-kind benchmark framework and challenge, designed to support the development and performance assessment of tissue tracking algorithms for surgery. This framework contains a collection of rules for tracking, metrics for analysis of performance, a data labelling tool and a curated dataset. This challenge is a sub-challenge of the Endoscopic Vision Challenge<sup>1</sup> organised in conjunction with the 25th International Conference on Medical Image Computing and Computer Assisted Intervention (MICCAI 2022). The whole dataset, benchmarking framework, and labelling tool are publicly available. These can be found at <https://surgt.grand-challenge.org/>.

<sup>1</sup>More info at: <https://endovis.grand-challenge.org/>

## 2. Dataset and Annotation

### 2.1. Data

The SurgT dataset is comprised of 157 stereo videos, with camera calibration parameters available, from 20 clinical cases. These videos were split into three subsets: (i) training - 125 videos from 12 cases; (ii) validation - 12 videos from 3 cases; and (iii) testing (hidden during the challenge) - 20 videos from 5 cases. Figure 1 shows sample images from all cases. Every case contains multiple videos from the same surgery, and each case corresponds to a different surgery. Across the dataset, the average duration of a video is 30 seconds, with a standard deviation of 10 seconds. The framerate of most videos is 25 Hz but there are a few cases with 30 Hz. The video resolutions also vary. While most cases have a resolution of  $1280 \times 1024$  pixels, there are videos with resolutions as low as  $360 \times 288$  pixels. Finally, most videos are compressed using H.264 encoding and a few have no compression.

The structural organization of SurgT’s dataset is illustrated in Figure 2. For each clinical case, a calibrated stereo endoscopic camera was used to capture the videos. The stereo camera calibration parameters are available for all the videos in the dataset, which can be used to rectify the stereo-frames. The main reason for making the stereo camera calibration parameters available is to allow the development of methods that track the soft-tissue using 3D information. The video data is not rectified by default to preserve the original videos. Code is provided for rectification.

#### 2.1.1. Sources of data

The dataset was generated using the following three sources: Hamlyn dataset (Giannarou et al., 2012), SCARED (Allan et al., 2021), and Kidney boundary dataset (Hattab et al., 2020).

Characteristics of the validation subset are presented in Table 1. On the validation subset, Case 1 is taken from SCARED (Allan et al., 2021), which captures a fresh porcine cadaver and therefore the scene is rigid and there are no deformations or movement besides the camera’s. Case 2 (Hattab et al., 2020) is from the Kidney boundary dataset, which captures an *in vivo* porcine abdominal kidney procedure. Case 3, captures a *in vivo* human

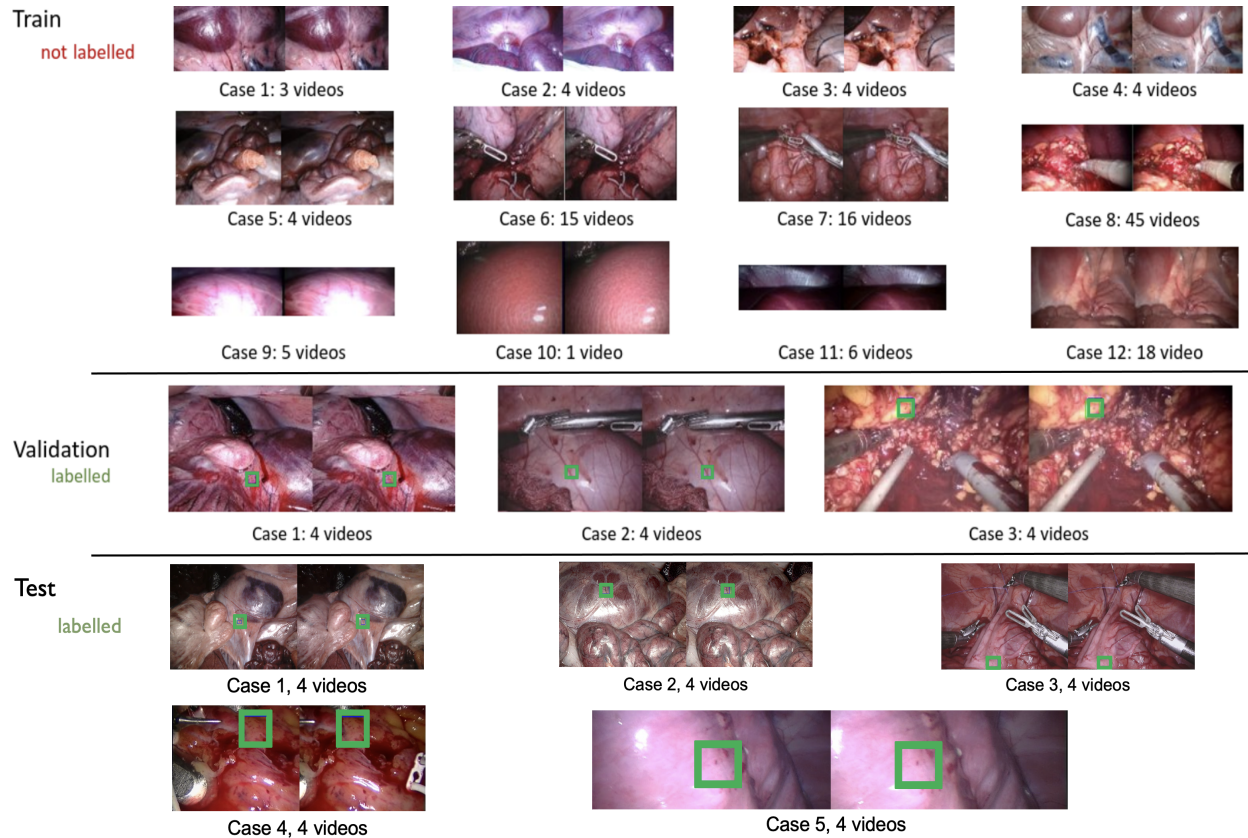


Figure 1: Sample images from all sources. Note that the training subset is not labelled, since SurgT’s goal is to encourage the development of **unsupervised** algorithms. Challenging conditions in the data include occlusions due to surgical instruments, specular highlights, deformation, blood or smoke; different resolutions; different video encodings; and different illumination conditions. Note that there are no videos of phantoms, and only videos from real surgeries and videos from a fresh porcine cadaver are included. Stereo camera calibration parameters and information regarding each surgery is also provided with each video.

surgery, concretely a Robotic-assisted Partial Nephrectomy (Ye et al., 2017).

Characteristics of the test subset are presented in Table 2. On the test subset, the first two cases were taken from SCARED (Allan et al., 2021). Case 3 (Hattab et al., 2020) from the Kidney boundary dataset. Case 4 (Stoyanov et al., 2005) an *in vivo* human Totally Endoscopic Coronary Artery Bypass (TECAB) graft. Lastly, case 5 (Mountney et al., 2010) was obtained in an *in vivo* porcine abdominal surgery with general camera motion and tissue-tool interaction.

## 2.2. Data annotation protocol

For the purpose of performance evaluation, the validation and test subsets were annotated. A labelling tool (Cartucho, 2022) was specifically created for this purpose. During data annotation with this tool, the objective for the annotator is to select a target keypoint (in both stereo images) and manually track and label it across the whole video. A bounding box for each keypoint is then automatically drawn around the point. The method for determining the size of the bounding box is explained in Section 2.3.

Prior to labelling, the annotator is advised to watch the entire video to determine a suitable keypoint to track.

Table 1: Description of the cases on the validation subset.

|  | Case 1               | Case 2                | Case 3            |
|--|----------------------|-----------------------|-------------------|
| <i>Source</i>                                    | (Allan et al., 2021) | (Hattab et al., 2020) | (Ye et al., 2017) |
| <i>Resolution</i><br><i>W x H [pixels]</i>       | 1280 x 1024          | 1280 x 1024           | 480 x 270         |
| <i>Framerate [Hz]</i>                            | 25                   | 30                    | 25                |
| <i>Deforming Tissue</i>                          | -                    | ✓                     | ✓                 |
| <i>Avg. 2D velocity</i><br><i>[pixels/frame]</i> | 3.2                  | 2.5                   | 1.0               |
| <i>Avg. 3D velocity</i><br><i>[mm/frame]</i>     | 0.63                 | 3.22                  | 1.94              |
| <i>% “ignore” frames</i>                         | 1                    | 28                    | 33                |
| <i>Avg. NCC score</i>                            | 0.97                 | 1.0                   | 0.97              |

Table 2: Description of the cases on the test subset.

|  | Case 1               | Case 2      | Case 3                | Case 4                  | Case 5                  |
|--|----------------------|-------------|-----------------------|-------------------------|-------------------------|
| <i>Source</i>                                    | (Allan et al., 2021) |             | (Hattab et al., 2020) | (Stoyanov et al., 2005) | (Mountney et al., 2010) |
| <i>Resolution</i><br><i>W x H [pixels]</i>       | 1280 x 1024          | 1280 x 1024 | 1280 x 1024           | 360 x 288               | 720 x 288               |
| <i>Framerate [Hz]</i>                            | 25                   | 25          | 30                    | 25                      | 25                      |
| <i>Deforming Tissue</i>                          | -                    | -           | ✓                     | ✓                       | ✓                       |
| <i>Avg. 2D velocity</i><br><i>[pixels/frame]</i> | 4.6                  | 6.2         | 1.6                   | 3.0                     | 5.8                     |
| <i>Avg. 3D velocity</i><br><i>[mm/frame]</i>     | 0.92                 | 0.65        | 0.16                  | 0.53                    | 1.65                    |
| <i>% “ignore” frames</i>                         | 7                    | 20          | 5                     | 0                       | 17                      |
| <i>Avg. NCC score</i>                            | 0.97                 | 0.94        | 0.99                  | 0.98                    | 0.99                    |

*W* width; *H* height; *Avg.* Average; *2D velocity* is the keypoint’s speed on the image plane; *3D velocity* is the keypoint’s speed when projected into 3D space. “*ignore*” frames are the ones flagged as difficult or where the bounding box is occluded/out-of-view; *NCC* Normalized Cross Correlation, computed using the anchor’s bounding box as template, and then comparing this template with all the subsequent ground truth bounding boxes of that video.



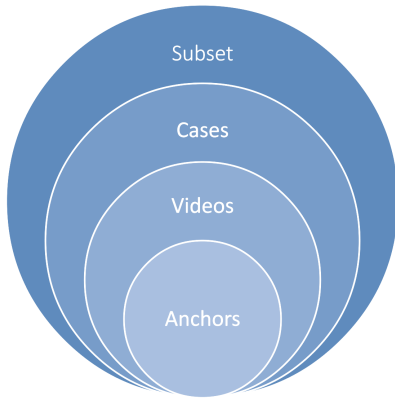


Figure 2: The SurgT dataset is comprised of training, validation and test subsets. Each subset contains all videos belonging to a number of cases. No cases are captured from the same surgery. Each case contains a series of videos, where each video contains a series of anchor points (i.e. the frames where the tracker is initialized along the video, explained later in Sec. 3.2). Note that if multiple bounding boxes were labelled per video, then there would be another layer between *Anchors* and *Videos*. Each bounding box would have its own set of anchors. In this challenge, a single bounding box was labelled per video, hence there was no need for a *Bounding box* layer.

Given the objective of the task, it is important to select suitable keypoints, bearing in mind that many factors can affect the difficulty, or even the possibility, of annotation. Once a suitable keypoint has been determined, the annotator would simply be required to select it continuously across the video, by clicking on both the left and right rectified images. The labelling tool ensures that the keypoint labelling between the stereo images obeys the epipolar line, as the tool automatically rectifies the stereo images. The labelling of the stereo images is along a horizontal line. After annotating each keypoint, the annotator is advised to check the label quality by looking back at the previous frame in the video sequence, ensuring that the same keypoint is labelled and that there was no labelling drift from the previous to the current frame. After a video has been fully annotated, the annotations are reviewed by another expert annotator, to ensure that fair and consistent annotations are provided for the challenge.

In the case where a keypoint is difficult to annotate within a frame, or causes conflicting opinions between annotators, a Boolean labelling flag *is\_difficult* is set, declaring the keypoint annotation (and hence the frame) as difficult. Frames flagged as difficult will not affect the

final ranking scores as later explained in the metric sections. Additionally, if the keypoint is occluded in either the left or the right stereo image (e.g., due to obstruction by surgical instruments), or if the keypoint moves outside of the field-of-view, then the annotator should change the Boolean labelling variable *is\_visible\_in\_both\_stereo*, which is *True* by default to declare that the keypoint is visible on both stereo images.

### 2.3. Estimation of bounding box size

A bounding box encodes a target region to be tracked. Therefore, if the target moves closer to the camera, the size of the corresponding bounding box should increase. Conversely, if the target moves away from the camera, the size of the bounding box should decrease. Therefore, to increase and decrease the size of the bounding box, the disparity information from the stereo annotation was used. Concretely, the disparity is the horizontal distance between the left bounding box’s centre and the right bounding box’s centre, on the rectified images. Using this disparity value, the keypoint is projected into the 3D space (using Eq. 6) and a virtual sphere with a radius of  $2.5\text{ mm}$  is defined around this 3D keypoint. This sphere is then projected onto the left and right images, creating elliptical contours on each stereo image. These elliptical contours are then enclosed by a bounding box, which is used to encode the position of the target tissue region. This process is illustrated in Figure 3. Using this method, the size of the bounding boxes adapt to the distance between the target and the camera as desired.

## 3. Benchmarking Metrics

The SurgT benchmarking Python toolkit is open-source and available at [https://github.com/Cartucho/SurgT\\_benchmarking](https://github.com/Cartucho/SurgT_benchmarking).

### 3.1. Performance evaluation protocol

The benchmarking metrics selected in SurgT follow the protocol to evaluate short-term trackers defined in the VOT2021 challenge (Kristan et al., 2021). The main reason for using the VOT metrics as a starting point was due to the maturity of the VOT2021 challenge (has been established since 2013) and for consistency.

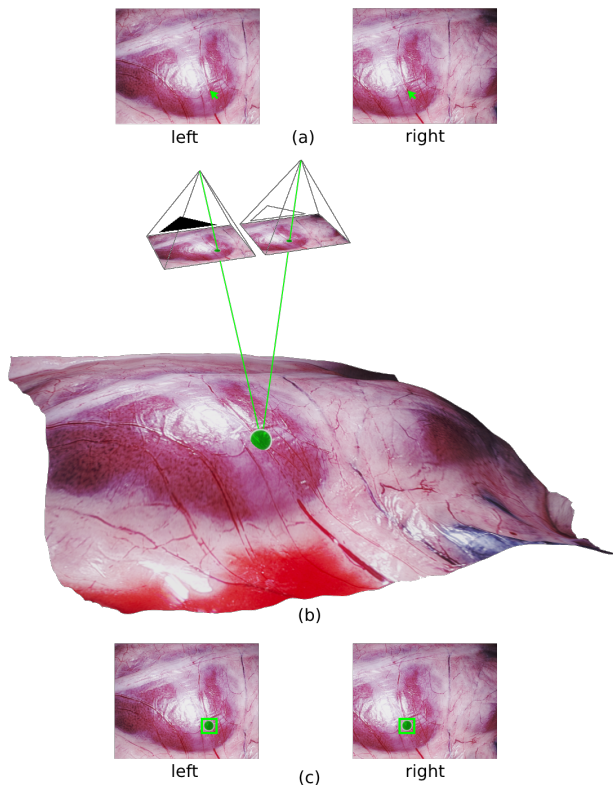


Figure 3: (a) The stereo-rectified images are annotated (green mouse cursors on top). (b) The stereo camera calibration parameters are used to project the selected keypoint into the 3D space and a virtual sphere is created around this 3D point. (c) The sphere is projected onto the 2D left/right image space and its contours are used to define the respective bounding boxes.

The main difference from SurgT is that VOT2021 is composed of natural videos tracking humans, cars, animals or other objects, while SurgT tracks soft-tissue surfaces. Besides that, adaptations were made to VOT’s metrics, to better suit the surgical context. For example, in SurgT, the videos are not played backwards during the evaluation stage, as done in VOT2021. The reason for this is that it is unnatural to play surgical videos backwards. For example, it is unrealistic to show reverse stitching or reverse resections, or for blood to be moving inwards to ruptured blood vessels. Another difference between SurgT and VOT2021 is that the metrics were extended to support the 3D evaluation of the trackers, leveraging the availability of calibration parameters in SurgT

stereo videos. In SurgT, the trackers are thus assessed, separately, in both 2D (Sec. 3.3) and 3D (Sec. 3.4). Another crucial difference between SurgT and VOT2021 is that the former includes a “*ignore*” label to flag frames where the target region is occluded or out of the camera’s field-of-view ( $is\_visible\_in\_both\_stereo = False$ ), or when any other visible issues are present such as motion blur ( $is\_difficult = True$ ). These differences are summarized in Tab. 3. The following sub-sections explain in detail the performance evaluation metrics used in SurgT.

### 3.2. Anchors for Tracker Initialization

The trackers are initialized at pre-defined anchor points, which are the target regions, encoded as left/right bounding boxes, that are provided as input to a tracking algorithm. The tracker’s task is to then output the target bounding box for the following sequential frames in the video, until the end of the video. After completing the video, the tracker is re-initialized using the same video, but this time starting at the next anchor point, as illustrated in Figure 4. Evaluation of a video is only finalized once the tracker has been initialized and assessed using all anchors of the video. Successive anchors were roughly spaced by 50 frames (as suggested by VOT (Kristan et al., 2021)), while always ensuring that anchor points are set on frames with clearly visible keypoints. In the test subset, there were, on average, 13 anchor points per video.

There are two main reasons for using anchor points and for spacing them in time: (i) it ensures that only suitable initial tracking targets are given, i.e. the target point is clearly visible (without blur or compression artefacts); (ii) it allows a more complete and reliable assessment of the tracker on each video, reducing the influence of individual frames in the evaluation and emphasising the video sequence as a whole. For example, if there is a tracking failure when initialized in the first anchor, it still has a chance of improving its score when initialized in the following anchor points.

### 3.3. Monocular metrics

The tracker’s task is to locate the target point, encoded in a bounding box, for all video frames following the anchor point initialization. If the target point is not visible in the image, then the tracker should identify this and give a classification output *None*. A target point is not visible

Table 3: Differences between SurgT and VOT2021 (Kristan et al., 2021).

| Challenge | <i>Backwards video</i> | <i>Stereo &amp; cam. param</i> | <i>3D scores</i> | <i>“Ignore” labelling</i> |
|-----------|------------------------|--------------------------------|------------------|---------------------------|
| VOT2021   | ✓                      | -                              | -                | -                         |
| SurgT     | -                      | ✓                              | ✓                | ✓                         |

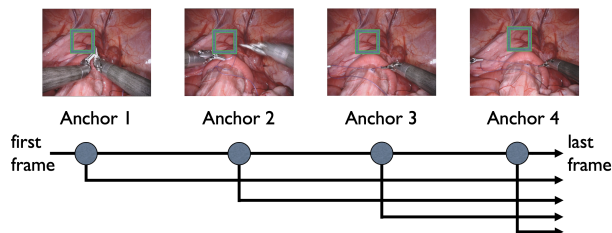


Figure 4: Anchor points used to initialize a tracker on a given video. The tracker is evaluated multiple times per video, each time initialized at a distinct anchor point and evaluated until the end of the video.

when, for example, the target is being occluded by a surgical instrument, or when the target is outside the camera’s field-of-the-view.

A frame is considered valid if the target point is both (i) visible and (ii) not difficult (see Sec. 2.2). Given the valid frames, the tracker’s performance is assessed by comparing the tracker’s bounding box prediction with the ground truth bounding box. The tracker is assessed for all subsequent valid frames until a tracking failure is detected (if it is ever triggered), or up to the video’s last valid frame.

### 3.3.1. 2D Tracking failure

For each anchor point, a 2D tracking failure is detected when the Intersection over Union (IoU), between the ground truth and predicted bounding box, is smaller than 0.1, for 10 consecutive frames. The target point is required to be tracked in both left and right stereo images. Therefore, 2D tracking failure can be triggered if the failure occurs in either the left or the right image. After the tracking failure, the 2D accuracy and 2D error scores are not updated further for that anchor sub-sequence. Conversely, the 2D robustness score is negatively affected by tracking failure since all subsequent frames are recorded as failed to be tracked.

### 3.3.2. Accuracy

For each anchor sub-sequence, the accuracy is the average IoU between the predicted and ground truth bounding boxes, before any tracking failure occurs:

$$IoU = \frac{Area\_Intersection}{Area\_Union} \quad (1)$$

$$Accuracy = \frac{1}{n} \sum_{i=1}^n IoU_i \quad (2)$$

where  $i$  is the frame index and  $n$  is the number of frames for which tracking has been successful and ground truth is available. For example, if there are a total of 1000 frames, and the 2D tracking failure is triggered in the last frame, it means that during the last 10 frames, the IoU score was  $< 0.1$ . Therefore, the accuracy will be calculated using the first 990 frames, which are the  $n$  frames before tracking failure occurs. Note that  $n$  only includes frames for which ground truth is available. Some frames, as explained in the annotation protocol (Sec. 2.2), were flagged as difficult ( $is\_difficult = True$ ) or as not visible ( $is\_visible\_in\_both\_stereo = False$ ), and thus these frames are ignored to ensure that they do not affect the accuracy score.  $n$  also does not include frames where the tracker made no prediction, since failure to predict an updated bounding box should not affect its accuracy score, only its robustness score.

### 3.3.3. 2D Error

For each anchor sub-sequence, the 2D error is the average distance (in *pixels*) between the centre of the predicted bounding box ( $p$ ) and the centre of the ground truth bounding box ( $gt$ ), before tracking failure occurs:

$$Error_{2D} = \frac{1}{n} \sum_{i=1}^n |p_{i_{2D}} - gt_{i_{2D}}| \quad (3)$$

where  $n$  is the number of frames for which ground truth is available and tracking successful. The  $n$  in the Accuracy score and  $Error_{2D}$  score equations are the same.

### 3.3.4. 2D Robustness

For each anchor sub-sequence, the 2D robustness score is given by the following ratio:

$$Robust_{2D} = \frac{n_{success\_frames_{2D}}}{n_{vis\_not\_diff} + n_{excess\_frames}} \quad (4)$$

where,  $n_{success\_frames_{2D}}$  is the number of tracked frames in which the IoU score is larger than 0.1, for both left and right bounding boxes;  $n_{vis\_not\_diff}$  is the number of frames where the target point was visible in both stereo images ( $is\_visible\_in\_both\_stereo = True$ ) and not marked as difficult ( $is\_difficult = False$ ); and  $n_{excess\_frames}$  is the number of frames where the tracker made a prediction but the target point was not visible in that frame ( $is\_visible\_in\_both\_stereo = False$ ). For example, if the tracker predicts a bounding box when the target point is outside the camera's field-of-view, the number of excessive frames is incremented. Similarly, if the tracker predicts a bounding box when the target point is occluded by a surgical instrument, the number of excessive frames is also incremented.

## 3.4. Stereo metrics

The 3D metrics are computed separately from the 2D ones, for each anchor point sequence.

### 3.4.1. Calculating the target point's 3D coordinates

Given that the input images are rectified, and the target point is being tracked in both left and right images, it is possible to project the target point into 3D. Specifically, given the central pixel position of both left and right bounding boxes, it is first possible to calculate the stereo disparity ( $d$ ) using:

$$d = u_{left} - u_{right} \quad (5)$$

where,  $u$  is the pixel coordinate along the epipolar line. Then, the disparity ( $d$ ) and the left central pixel coordinate

( $u_{left}, v_{left}$ ) can be used to project the point into 3D space, using the stereo calibration parameters as follows:

$$s \begin{bmatrix} X \\ Y \\ Z \\ 1 \end{bmatrix} = \begin{bmatrix} 1 & 0 & 0 & -c_x \\ 0 & 1 & 0 & -c_y \\ 0 & 0 & 0 & f \\ 0 & 0 & -\frac{1}{b} & 0 \end{bmatrix} \begin{bmatrix} u_{left} \\ v_{left} \\ d \\ 1 \end{bmatrix} \quad (6)$$

where,  $c_x$  and  $c_y$  represent the optical centre,  $f$  the focal length,  $b$  the baseline of the rectified cameras, and  $s$  an arbitrary scale factor. This equation is applied twice, calculating the predicted and ground truth 3D points, respectively, from the predicted and ground truth bounding boxes.

### 3.4.2. 3D Tracking Failure

As previously mentioned, 2D and 3D metrics are calculated separately. Therefore, 3D tracking failure detection is also separate from 2D tracking failure. For each anchor sub-sequence, a 3D tracking failure is detected when the distance between the predicted and ground truth 3D target positions (3D error) is larger than 10 *cm* or when the disparity is  $\leq 0$  for ten consecutive frames. Both conditions can be used together; for example, the tracker may have a 3D error  $> 10$  *cm* for five frames, and then get a negative disparity for the next five frames, which would still trigger a 3D tracking failure.

### 3.4.3. 3D Error

For each anchor sub-sequence, the 3D error is the average distance in *mm* between the predicted ( $p$ ) and the ground truth ( $gt$ ) bounding boxes, before 3D tracking failure occurs:

$$Error_{3D} = \frac{1}{n} \sum_{i=1}^n |p_{i_{3D}} - gt_{i_{3D}}| \quad (7)$$

where,  $n$  is the number of frames before 3D tracking failure on which the disparity is  $\geq 0$ . Note that, similarly to the 2D metric, the set  $n$  does not include frames that are marked as difficult ( $is\_difficult = True$ ) or in which the target is not visible ( $is\_visible\_in\_both\_stereo = False$ ).

#### 3.4.4. 3D Robustness

For each anchor sub-sequence, the 3D robustness score is given by the following ratio:

$$Robust_{3D} = \frac{n\_success\_frames_{3D}}{n\_vis\_not\_diff + n\_excess\_frames} \quad (8)$$

where,  $n\_success\_frames_{3D}$  is the number of tracked frames in which the 3D error is smaller or equal to 10 cm, and the disparity is positive. The other two variables,  $n\_vis\_not\_diff$  and  $n\_excess\_frames$ , are the same as the ones used for the 2D robustness score.

#### 3.5. Weighted Average of the Results

All final scores for each subset, case, or video on the aforementioned 2D and 3D metrics are obtained using weighted averages. For example, the 2D accuracy of a video, which contains multiple anchors, is obtained using:

$$Video_{Accuracy} = \sum_{i=1}^k \frac{Accuracy_i \times n_i}{n_{video}} \quad (9)$$

where,  $k$  is the number of anchors in that video,  $Accuracy_i$  is the accuracy of anchor sub-sequence  $i$ ,  $n_i$  is the number of frames in sub-sequence  $i$  before 2D tracking failure is detected, and  $n_{video} = \sum_{i=1}^k n_i$ .

For a given case, the accuracy is mathematically defined as:

$$Case_{Accuracy} = \sum_{i=1}^m \frac{Video_{Accuracy}_i \times n_{video_i}}{n_{case}} \quad (10)$$

where,  $m$  is the number of videos per case and  $n_{case} = \sum_{i=1}^m n_{video_i}$ .

Finally, for the validation or test subsets, the accuracy is estimated as:

$$Subset_{Accuracy} = \sum_{i=1}^l \frac{Case_{Accuracy}_i \times n_{case_i}}{n_{subset}} \quad (11)$$

where,  $l$  is the number of cases per subset and  $n_{subset} = \sum_{i=1}^m n_{case_i}$ .

#### 3.6. Expected Average Overlap (EAO)

Although the aforementioned 2D and 3D metrics are used to assess different characteristics of the tracker, ultimately it is the Expected Average Overlap (EAO) metric that determines the overall quality of the tracker and is therefore used to rank the different trackers. The EAO is computed by averaging the IoU score from the merged sequence ( $IoU_{subset}$ ) between  $N_{min}$  and  $N_{max}$ , excluding all “ignore” frames:

$$EAO = \frac{1}{N_{max} - N_{min}} \sum_{i=N_{min}}^{N_{max}} IoU_{subset_i} \quad (12)$$

where,  $N_{min}$  and  $N_{max}$  are defined as the average length of all video sequences ( $IoU_{video_i} \pm$  one standard deviation of these lengths). The same  $N_{min}$  and  $N_{max}$  values were applied to all trackers during evaluation.  $N_{min}$  and  $N_{max}$  for the test subset highlight the EAO scoring region in Fig. 5.  $EAO \in [0, 1]$ , where a result of 1 is the perfect score. To obtain  $IoU_{subset}$  the score of all anchor sub-sequences are merged for each video, and then the scores of all videos of a subset are also merged into  $IoU_{subset}$ .

##### 3.6.1. Anchor IoU

Each anchor point, defined in Sec. 3.2, creates a sub-sequence of the full video. In each sub-sequence, the IoU score is calculated for each frame. For a demonstrative example, we define a video containing two anchor points and the following IoU scores for the two sub-sequences:

$$IoU_{s1} = [1, 0.8, 0.6, 0.5, \text{“ignore”}, \dots, 0], len = 100$$

$$IoU_{s2} = [1, 1, 1, \text{“ignore”}, \text{“ignore”}, \dots, 0], len = 80$$

As illustrated in this example, usually the IoU scores start with larger values (close to 1), since the tracker has just been initialized, and decrease as the video sequence progresses due to tracking drift (getting as low as 0). The scores of image frames that are flagged as difficult or in which the target is not visible are recorded as “ignore”, since these frames should not affect the final score.

Although not exemplified in the previous sub-sequences, if a 2D tracking failure is detected, then all subsequent frames of a given sub-sequence are set to 0, since the tracker already failed. This means that if the tracker drifts and 2D tracking failure is triggered, then the EAO score gets negatively impacted due to the trailing zeros.

### 3.6.2. Video IoU

After all anchor sub-sequences have been processed and the results recorded, an average is computed to obtain an IoU sequence for the video. In this simplified example, we would obtain (given  $IoU_{s1}$  and  $IoU_{s2}$ ):

$$IoU_{video_1} = [1, 0.9, 0.8, 0.5, \text{"ignore"}, \dots, 0], len = 100$$

Note that, since in the 4<sup>th</sup> frame  $IoU_{s1} = 0.5$  and  $IoU_{s2} = \text{"ignore"}$ , then the 4<sup>th</sup> frame of  $IoU_{video_1} = 0.5$ . If all the scores of a frame are recorded as “ignore” (like in the 5<sup>th</sup> frame), then the respective frame in  $IoU_{video_1}$  is also set to “ignore”. Also note that when merging scores, the length of the largest sub-sequence is kept to merge all the scores from the anchors of that video (in this case,  $len = 100$ ).

Let us now assume a second video, either from the same clinical case or from another case, with the following scores:

$$IoU_{video_2} = [1, 1, 1, 0, 0, \dots, 0], len = 200$$

Using all recorded IoU scores, a single merged sequence ( $IoU_{dataset}$ ) score can be calculated using all videos (here,  $IoU_{video_1}$  and  $IoU_{video_2}$ ). Note that each video contributes exactly with a single sequence of IoU scores, independently of the number of anchors in that video. This is to avoid a scenario where a video with more anchors has a bigger contribution towards the final EAO score when compared to a video with fewer anchors. In this simplified example, the subset score would be:

$$IoU_{subset} = [1, 0.95, 0.9, 0.25, 0, \dots, 0], len = 200$$

Note that, again, the “ignore” frame of  $video_1$  was ignored (its 5<sup>th</sup> element). If both videos had “ignore” in the 5<sup>th</sup> frame, then “ignore” would still show up on the 5<sup>th</sup> frame of  $IoU_{subset}$ , but this would not affect the final EAO score as explained later. Also note that, the length of  $IoU_{subset}$  is as large as the largest video sequence (in this case  $len(IoU_{video_2}) = 200$ ). This implies that larger videos, with more frames, may have a larger contribution to the final EAO score than smaller videos. However, this effect is reduced given that the final EAO score is computed over a pre-defined range of frames.

### 3.7. Winner identification protocol

The teams were ranked according to their EAO scores on the test subset as shown in Fig. 6.

## 4. Baseline methods for comparison

Two baseline bounding box trackers were used to compare the results obtained by the participants namely, the CSRT (Sec. 4.1) - a traditional computer vision method, and the TransT (Sec. 4.2) - a deep learning method trained only on natural scenes.

### 4.1. [CSRT] Baseline - traditional computer vision

OpenCV’s Channel and Spatial Reliability Tracker (CSRT) (Lukežic et al., 2017) is provided on the SurgT benchmarking code by default. The idea is for the participating teams to use it as a baseline for comparison, and to monitor the performance of their own algorithms during development. CSRT is a Discriminative Correlation Filters (DCF) tracker that adapts the filter response to the target region that is suitable for tracking (spatial reliability), in addition to using all the colour channels for localizing the bounding box in the next frame (channel reliability) (Lukežic et al., 2017).

### 4.2. [TransT] Baseline - natural scenes deep learning

Transformer Tracking (TransT) (Chen et al., 2021) is a state-of-the-art tracker using an attention-based feature fusion approach, inspired by (Vaswani et al., 2017). To be used as a baseline tracker, TransT was trained on the VOT2020 dataset (Kristan et al., 2020) until convergence, using ground truth bounding boxes of natural scenes such as moving objects, humans, animals, and others. No surgical data was used during the training of TransT. This is used to assess whether a supervised deep learning method, trained on an irrelevant dataset, can generalise well onto SurgT.

## 5. Challenge submissions

### 5.1. [Jmees] Company name: Jmees, Japan

Jmees’s tracking method is composed of an (a) **tracking** part and a (b) **correction** part. For (a) **tracking**, the CSRT tracker (Lukežič et al., 2018) was used along with template matching using the initial anchor’s bounding box as a template. For (b) **correction**, three types of correction were applied. First, the stereo disparity is calculated from the rectified images, between the centre of the left/right bounding boxes. The ratio between the disparity of the

initial frame and that of the updated frame is used to scale the size of the updated bounding boxes. Second, surgical instrument segmentation is used to judge the occlusion. If an occlusion is detected then tracking failure is determined. The segmentation was trained using a supervised learning method and a publicly available dataset for surgical instrument segmentation (Maier-Hein et al., 2014). Third, back-tracking and template matching between current and previous frames are used for the validity assessment of the tracking. When the result of the assessment is not valid, then tracking failure is flagged.

5.2. *[ETRI] Company name: Electronics and Telecommunications Research Institute, Republic of Korea*

ETRI's tracker is based on the Unsupervised Deep Tracking (UDT) Wang et al. (2021), which is built on a discriminant correlation filter. UDT is an unsupervised learning method, trained using crops of the upper central image regions. This method learns to track by comparing adjacent frames with forward and backward predictions. In ETRI's method, the template is cropped (input image to a neural network) and search patches from two consecutive frames conducting forward tracking and backward verification - which is why there is no need for ground truth, as the patches are predicted on the raw images, in adjacent frames. The upper centre part of the image was used as the target because it was assumed that there should be minimal movement and therefore it is unlikely that the target would move out of the pre-defined cropped region, in a short period. Additionally, the upper centre was used, instead of the centre, to avoid issues with surgical tools and occlusions. A dataset was created using these cropped images and split into a training and validation subset in a 90:10 ratio. The difference between the initial bounding box and the predicted bounding box formulates a consistency loss for network learning. In ETRI's method, the comparison was performed within 1 to 4 frames - choosing one to four patches as the template and the remaining as search patches. The obtained weights were learned from scratch on SurgT's training subset, without the use of any pre-trained weights.

5.3. *[MEDCVR] Medical Computer Vision and Robotics lab, University of Toronto, Canada*

MEDCVR's method is based on TransT (Chen et al., 2021), a Siamese-based tracker. TransT solves the prob-

lem that correlation filters in Siamese-based trackers tend to lose semantic information and fall into local optima through an attention-based feature fusion network. The default TransT was trained until convergence on the VOT2020 dataset (Kristan et al., 2020), which does not contain any surgical data. Then, unsupervised training on the feature extraction layers was used to tune TransT to surgical data and improve accuracy, using SurgT's training subset. Inspired by previous works which do self-supervision by predicting rotation angles and context reconstruction (He et al., 2022), two proxy tasks were exploited: masked volume inpainting and image rotation. The masked volume inpainting is motivated by prior work which focused on 2D images (Pathak et al., 2016). The rotation prediction task predicts the angle categories by which the input sub-volume is rotated.

5.4. *[SRV] Surgical Robot Vision research group, University College London, United Kingdom*

SRV tackled this problem as a regression machine learning task, with images plus an initial bounding box as input and bounding box movement as output. Concretely, a receptive field twice as big as the initial bounding box is created. This receptive field defines the image region to where the bounding box can move from one frame to the next. After predicting this movement, a new receptive field is created for every two subsequent frames. The purpose of SRV's network is to estimate the bounding box's displacement. As an unsupervised task, spatial features from the input must be extracted without ground truth. A masked auto-encoder (MAE) (He et al., 2022), with pre-trained weights, was applied as a feature encoder. The pre-trained weights achieved a good reconstruction on the SurgT training subset, which indicates its good representation capability on this data and, hence, does not require further fine-tuning. Also, a 'goal' image (Andrychowicz et al., 2017) was introduced to represent the region of interest and guides the network to discover spatial differences. This 'goal' is also encoded by the same MAE encoder and concatenated with the bounding box feature. The two MAE concatenated features are then provided as input to a regression model (three layers of a vision transformer block (Dosovitskiy et al., 2020) plus two fully connected layers) to predict the updated location of the bounding box. This model is trained by augmenting randomly sampled bounding boxes and frames



from the SurgT training subset. For this augmentation, a random 2D translation displacement is applied to the sampled images. These displacements are known and can be used as the ground-truth signal for training the regression model. The network takes the augmented images and compares them with the ‘goal’ image to predict the displacements which can move the bounding box back to the original image. During inference, the ‘goal’ image is initialised with the receptive field around the target bounding box in the first frame. The extracted feature vector from the ‘goal’ receptive field is updated with every new frame using the following momentum equation:  $Goal_{k+1} = mGoal_k + (1 - m)newGoal$ , where,  $newGoal$  is the feature extracted from the receptive field around the current bounding box estimation and  $m$  is a tenable momentum parameter. The similarity between  $mGoal_k$  and  $newGoal$  is measured with mean square error. When  $similarity < 0.4$ , representing occlusion or poor tracking,  $m=1$  otherwise,  $m=0.95$ . On low-resolution videos, the tracking trajectory can suffer from jitters. Therefore, a Kalman filter designed for 2D tracking (Patel and Thakore, 2013) is used to refine the network’s regression result.

#### 5.5. [KIT] Karlsruhe Institute of Technology, Germany

This team proposed a CNN feature map tracker, consisting of three main components: feature map generation, similarity approximation and distance measurement. First, a feature map for a specific target region in the image is generated based on a ResNet50 backbone, which was pre-trained on the ImageNet dataset (Deng et al., 2009). Second, similar regions in subsequent frames are searched, creating a set of potential bounding box candidates. These are derived by exploring the surroundings of the bounding box given a predefined step-width. Third, the candidate feature maps are quantitatively compared with the target feature map based on the cosine distance metric to find the most suitable one.

## 6. Post-challenge submissions

### 6.1. [RIWolink] Company name: RIWolink GmbH, Germany

RIWolink’s tracking method is based on the UDT tracker (Wang et al., 2019). A siamese convolutional

neural network is used to extract features from a template patch and two search patches. Tracking is implemented with Discriminative Correlation Filters regressing the search features to a Gaussian response centred at the bounding box centre. Forward and subsequent backward tracking using a pseudo label provides an unsupervised consistency loss. The unsupervised training of the model is executed on the SurgT unlabeled training data. Left and right sequences are treated as different training samples. Adding cholec80 data (Twinanda et al., 2017) to the unsupervised training improved the validation EAO metric by 0.05. Adding even more unlabeled data lead to a decrease in the validation metrics. The model is trained for 100 epochs with a batch size of 128, a learning rate of  $1 \times 10^{-3}$  and a weight decay of  $5 \times 10^{-5}$ . Images are pre-processed as image patches of size  $125 \times 125$  with mean of training split subtracted. Forward-backward error (Kalal et al., 2010) is used to detect tracking failures. The best model is chosen with the EAO metric evaluated on the SurgT validation subset.

### 6.2. [ICVS-2Ai] Collaboration between Life and Health Sciences Research Institute (ICVS) and Applied Artificial Intelligence Laboratory (2Ai), Portugal

This method is based on ARFlow, an unsupervised dense optical flow estimator introduced in Liu et al. (2020). ARFlow builds on the PWC-net method (Sun et al., 2018), incorporating heavy augmentation as a self-supervised regularization technique. To train this model, pairs of consecutive images from the SurgT train subset were randomly cropped to a square of size equal to the smallest dimension and resized to  $256 \times 256$  pixels. Since no ground truth data is available, the model was trained using two losses: a photometric loss applied on non-occluded pixels (estimated using a forward-backward checking method) of the reconstructed image of the current frame (obtained by wrapping the subsequent frame with the predicted optical flow); and a regularization loss term to smooth the predicted optical flow and reduce ambiguity in textureless patterns (Liu et al., 2020). The training was performed with the AdamW optimizer over 40 epochs, using a constant learning rate schedule. The epoch with the best validation EAO score was then selected. During inference, this model was used to track the centroid of the target bounding box. To do so, the current and next frames are center-cropped on the current centroid

point (with size  $256 \times 256$  without resizing) and fed to the model. The displacement at the location of the centroid is used to update the bounding box position. In its turn, the disparity between left-right images is estimated and used to update the bounding box size (keeping the proportion calculated at the initial frame of the video). This process is consecutively repeated for every pair of frames of a given video.

## 7. Challenge results

The detailed results on each of the test cases are presented in Tab. 4, according to the benchmarking metrics defined in Sec. 3. This table is divided into two sub-tables, one for 2D and another one for 3D scores. All test scores, on all cases, are then averaged into Tab. 6. Similarly, the average scores on the validation subset are presented in Tab. 5. These tables summarize the 2D and 3D scores, plus the aggregated EAO score. The associated EAO curves for the test subset are shown in Fig. 5. The final rankings can be found in Fig. 6, with the associated 2D accuracy vs. robustness shown in Fig. 7.

## 8. Discussion

Regarding the performance evaluation results, it is noticeable that the overall scores on the validation subset (Tab. 5) are lower than the scores on the test subset (Tab. 6). The most evident difference between the two subsets is the average 3D velocity of the bounding box, which is greater in the validation subset (highlighted in blue in Tab. 1 and Tab. 2). Therefore, it is hypothesised that the velocity of the keypoint in the 3D space is related to the tracking performance. Nevertheless, the teams ranking on the validation subset is similar to the ranking on the test subset. This indicates that there was no team that overfitted to the validation subset since the relative scores were appropriately translated to the test scores.

Concretely, on the test subset (Tab. 4), the most stand-out point to be noted is that case 5 seems to be the most challenging, registering the lowest performance for all contesting teams. One hypothesis is that this may be due to: (1) the large average 3D velocity of the bounding box ( $1.65 \text{ mm/frame}$ , shown in Tab. 2), (2) the large motion of the bounding box over the image plane (shown in

Fig. 8), and (3) the low texture in the image region around the bounding box (shown in Fig. 9).

From the overall results, it is clear that it is possible to develop tracking algorithms using unsupervised deep learning frameworks. However, there is clearly scope for improvement. Unlike other vision applications, for this challenge, the best submission (Jmees team) utilised the baseline CSRT as the main component of their algorithm, instead of deep learning. This goes against what is generally expected, as most computer vision topics have now been dominated by deep learning. We hope this finding stimulates interest in this problem for future research work. In fact, only ICVS-2Ai’s tracker was able to beat the CSRT tracker via unsupervised learning.

The other baseline tracker, TransT, was used to check whether it is possible to train a supervised tracker on non-surgical datasets, given that there are many available natural scene datasets with ground truth annotations. However, the low scores on both validation and test subsets indicate that TransT does not generalize well onto SurgT. This highlights the need for unsupervised methods for surgical data, given the lack of ground truth.

It is worth noting that all submissions track the left view’s bounding box separately from the right view’s bounding box. It would be interesting to explore whether a tracker that jointly estimates the bounding boxes on both left and right views would obtain better results. This assumes that the left and right cameras are accurately calibrated and synchronized. In our dataset, all stereo videos are provided with stereo camera calibration parameters. The quality of these parameters was checked by verifying that the keypoints respect the epipolar geometry constraint after stereo rectification of the images.

All the videos, and stereo calibration parameters, provided on the SurgT dataset were collected from previously existing datasets. Half of these videos capture surgical procedures on fresh porcine cadavers and the other half on in vivo human procedures. For a tracker to be used in real surgeries, there is an imperative need for the collection of more data and annotations of real in vivo human procedures - which are much more dynamic and complex than data from cadaver experiments. As future work, SurgT is to be further extended with videos from more in vivo clinical cases.

Finally, the two thresholds that were used for triggering 2D and 3D tracking failure, respectively of  $IoU < 0.1$

Table 4: Case breakdown of tracking scores on the test subset.

| Method    | Test 2D Case Scores |         |                   |         |         |                   |         |         |                   |         |         |                   |         |         |                   |
|-----------|---------------------|---------|-------------------|---------|---------|-------------------|---------|---------|-------------------|---------|---------|-------------------|---------|---------|-------------------|
|           | Case 1              |         |                   | Case 2  |         |                   | Case 3  |         |                   | Case 4  |         |                   | Case 5  |         |                   |
|           | Rob. 2D             | Acc. 2D | Error 2D [pixels] | Rob. 2D | Acc. 2D | Error 2D [pixels] | Rob. 2D | Acc. 2D | Error 2D [pixels] | Rob. 2D | Acc. 2D | Error 2D [pixels] | Rob. 2D | Acc. 2D | Error 2D [pixels] |
| Jmees     | 0.92                | 0.76    | 7±3               | 0.89    | 0.77    | 7±3               | 0.88    | 0.88    | 5±2               | 0.94    | 0.90    | 3±1               | 0.70    | 0.75    | 5±3               |
| ICVS-2Ai* | 0.94                | 0.76    | 9±4               | 0.84    | 0.79    | 9±6               | 0.91    | 0.88    | 5±3               | 1.0     | 0.90    | 3±1               | 0.65    | 0.72    | 8±5               |
| CSRT**    | 0.92                | 0.72    | 7±3               | 0.87    | 0.77    | 8±3               | 0.87    | 0.81    | 5±2               | 1.0     | 0.85    | 3±1               | 0.70    | 0.68    | 6±3               |
| RIWOlink* | 0.89                | 0.66    | 9±5               | 0.71    | 0.78    | 9±6               | 0.85    | 0.86    | 3±1               | 0.99    | 0.69    | 10±5              | 0.55    | 0.59    | 9±6               |
| ETRI      | 0.88                | 0.56    | 21±13             | 0.82    | 0.69    | 14±10             | 0.85    | 0.82    | 7±3               | 0.94    | 0.73    | 7±4               | 0.49    | 0.60    | 10±6              |
| MEDCVR    | 0.74                | 0.54    | 7±5               | 0.65    | 0.48    | 16±12             | 0.82    | 0.68    | 4±4               | 0.77    | 0.61    | 10±7              | 0.46    | 0.57    | 6±4               |
| SRV       | 0.39                | 0.49    | 27±13             | 0.19    | 0.55    | 16±11             | 0.71    | 0.80    | 11±6              | 0.98    | 0.69    | 13±5              | 0.07    | 0.56    | 22±12             |
| TransT**  | 0.72                | 0.46    | 18±4              | 0.64    | 0.42    | 24±10             | 0.82    | 0.61    | 16±4              | 0.79    | 0.61    | 11±7              | 0.47    | 0.48    | 11±4              |
| KIT       | 0.26                | 0.61    | 19±13             | 0.17    | 0.61    | 23±17             | 0.81    | 0.84    | 9±7               | 0.84    | 0.71    | 11±6              | 0.16    | 0.58    | 20±10             |

| Method    | Test 3D Case Scores |               |         |               |         |               |         |               |         |               |         |               |         |               |
|-----------|---------------------|---------------|---------|---------------|---------|---------------|---------|---------------|---------|---------------|---------|---------------|---------|---------------|
|           | Case 1              |               |         | Case 2        |         |               | Case 3  |               |         | Case 4        |         |               | Case 5  |               |
|           | Rob. 3D             | Error 3D [mm] | Rob. 3D | Error 3D [mm] | Rob. 3D | Error 3D [mm] | Rob. 3D | Error 3D [mm] | Rob. 3D | Error 3D [mm] | Rob. 3D | Error 3D [mm] | Rob. 3D | Error 3D [mm] |
| Jmees     | 1.0                 | 2±1           | 0.85    | 2±1           | 0.93    | 1±1           | 0.95    | 1±1           | 0.99    | 5±34          | 0.72    | 5±4           | 0.72    | 5±4           |
| ICVS-2Ai* | 0.98                | 4±2           | 0.84    | 1±1           | 0.94    | 1±2           | 1.0     | 1±1           | 1.0     | 3±3           | 0.71    | 6±6           | 0.71    | 6±6           |
| CSRT**    | 0.91                | 5±4           | 0.83    | 2±1           | 0.93    | 1±1           | 1.0     | 1±1           | 1.0     | 5±34          | 0.78    | 9±16          | 0.78    | 9±16          |
| RIWOlink* | 0.96                | 7±4           | 0.81    | 6±5           | 0.93    | 1±1           | 0.99    | 1±1           | 0.99    | 11±7          | 0.72    | 11±7          | 0.72    | 11±7          |
| ETRI      | 0.97                | 6±4           | 0.90    | 7±6           | 0.94    | 2±3           | 1.0     | 2±3           | 1.0     | 13±13         | 0.71    | 13±13         | 0.71    | 13±13         |
| MEDCVR    | 0.90                | 8±22          | 0.75    | 20±125        | 0.88    | 2±9           | 0.92    | 10±62         | 0.92    | 14±24         | 0.67    | 14±24         | 0.67    | 14±24         |
| SRV       | 0.66                | 16±13         | 0.37    | 16±12         | 0.96    | 3±3           | 1.0     | 2±1           | 1.0     | 18±66         | 0.46    | 18±66         | 0.46    | 18±66         |
| TransT**  | 0.91                | 23±8          | 0.82    | 24±53         | 0.92    | 6±14          | 0.92    | 10±56         | 0.92    | 31±26         | 0.70    | 31±26         | 0.70    | 31±26         |
| KIT       | 0.68                | 20±16         | 0.70    | 23±14         | 0.97    | 2±2           | 1.0     | 6±5           | 1.0     | 20±19         | 0.68    | 20±19         | 0.68    | 20±19         |

\* post-challenge submission.

\*\* baseline method.

Table 5: Challenge validation subset scores.

| <b>Validation</b> |                |                |                             |                |                         |            |
|-------------------|----------------|----------------|-----------------------------|----------------|-------------------------|------------|
| <b>Method</b>     | <i>Rob. 2D</i> | <i>Acc. 2D</i> | <i>Error 2D</i><br>[pixels] | <i>Rob. 3D</i> | <i>Error 3D</i><br>[mm] | <b>EAO</b> |
| Jmees             | 0.724          | 0.795          | 5.5 ± 3.2                   | 0.741          | 2.5 ± 2.0               | 0.314      |
| CSRT**            | 0.705          | 0.766          | 5.6 ± 3.1                   | 0.743          | 3.9 ± 3.6               | 0.292      |
| ICVS-2Ai*         | 0.687          | 0.826          | 4.8 ± 2.4                   | 0.765          | 7.3 ± 5.9               | 0.285      |
| ETRI              | 0.635          | 0.675          | 14.1 ± 8.0                  | 0.720          | 8.6 ± 9.3               | 0.206      |
| RIWOLink*         | 0.665          | 0.698          | 9.5 ± 4.9                   | 0.749          | 6.8 ± 6.0               | 0.203      |
| SRV               | 0.397          | 0.686          | 11.7 ± 7.1                  | 0.721          | 11.9 ± 12.7             | 0.131      |
| MEDCVR            | 0.436          | 0.614          | 7.0 ± 5.6                   | 0.638          | 18.4 ± 107.9            | 0.110      |
| KIT               | 0.375          | 0.672          | 12.8 ± 8.0                  | 0.698          | 17.2 ± 12.8             | 0.103      |
| TransT**          | 0.410          | 0.528          | 13.1 ± 4.1                  | 0.673          | 23.1 ± 25.8             | 0.095      |

\* post-challenge submission; *Rob.* robustness; *Acc.* accuracy.

\*\* baseline method.

Table 6: Challenge test subset scores.

| <b>Test</b>   |                |                |                             |                |                         |            |
|---------------|----------------|----------------|-----------------------------|----------------|-------------------------|------------|
| <b>Method</b> | <i>Rob. 2D</i> | <i>Acc. 2D</i> | <i>Error 2D</i><br>[pixels] | <i>Rob. 3D</i> | <i>Error 3D</i><br>[mm] | <b>EAO</b> |
| Jmees         | 0.868          | 0.818          | 5.3 ± 2.4                   | 0.878          | 2.7 ± 1.9               | 0.583      |
| ICVS-2Ai*     | 0.872          | 0.816          | 6.7 ± 3.5                   | 0.901          | 2.6 ± 2.3               | 0.573      |
| CSRT**        | 0.872          | 0.769          | 5.7 ± 2.6                   | 0.894          | 3.3 ± 3.8               | 0.563      |
| RIWOLink*     | 0.807          | 0.737          | 8.0 ± 4.5                   | 0.894          | 5.8 ± 9.2               | 0.433      |
| ETRI          | 0.802          | 0.693          | 12.1 ± 7.4                  | 0.909          | 5.7 ± 5.2               | 0.405      |
| MEDCVR        | 0.702          | 0.509          | 7.9 ± 5.8                   | 0.832          | 9.2 ± 39.7              | 0.302      |
| SRV           | 0.476          | 0.681          | 15.4 ± 7.5                  | 0.710          | 8.5 ± 13.7              | 0.293      |
| TransT**      | 0.701          | 0.529          | 16.3 ± 5.1                  | 0.861          | 17.3 ± 26.7             | 0.274      |
| KIT           | 0.465          | 0.747          | 12.5 ± 8.0                  | 0.810          | 11.9 ± 9.5              | 0.223      |

\* post-challenge submission; *Rob.* robustness; *Acc.* accuracy.

\*\* baseline method.

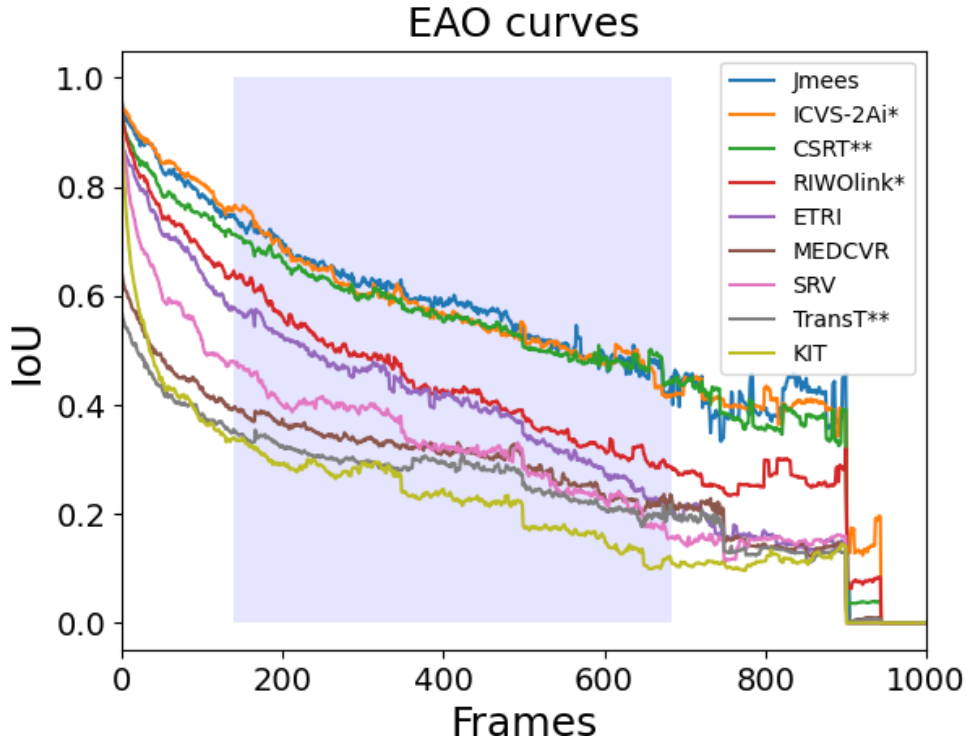


Figure 5: EAO curves for each participating team on the test subset. Highlighted in blue is the range of frames which contribute to the EAO score, used for final ranking.

and 3D error  $> 10$  cm are too large for robotic surgery. These values should be reduced for later editions of this challenge.

## 9. Conclusions

This paper introduces the SurgT challenge, which is part of the Endoscopic Vision Challenge, organised in conjunction with MICCAI2022. First, the SurgT benchmark framework is introduced. A framework is proposed for evaluating and ranking the performance of tissue-tracking algorithms applied to surgical videos, for both monocular and stereo scenarios. This is expected to be used in the future as the standard benchmark framework for research and development of soft-tissue tracking algorithms. As this is a novel application, a dataset was curated for this work, focusing primarily on the annotation

of keypoints for the validation of tracking methods. The data and code, for both benchmarking and labelling, can be found at <https://surgt.grand-challenge.org/>. The aim of this challenge was to investigate unsupervised algorithms for soft-tissue tracking. The challenge attracted 5 teams, with 2 further post-challenge team submissions. The main takeaway from this challenge is that it is possible to develop tracking algorithms using unsupervised deep learning frameworks to track soft-tissue.

### 9.1. CRediT authorship contribution statement

**João Cartucho:** Conceptualization, Methodology, Software, Resources, Data Curation, Formal analysis, Investigation, Validation, Visualization, Funding acquisition, Writing - Review & Editing, Project administration.  
**Alistair Weld:** Conceptualization, Methodology, Software, Data Curation, Formal analysis, Investigation, Vali-

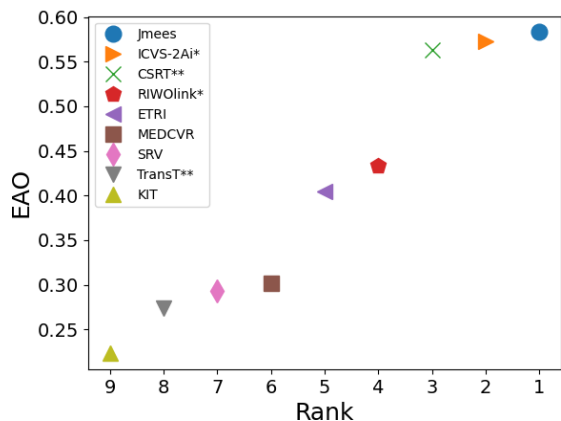


Figure 6: EAO score vs. rank of each contestant on the test subset.

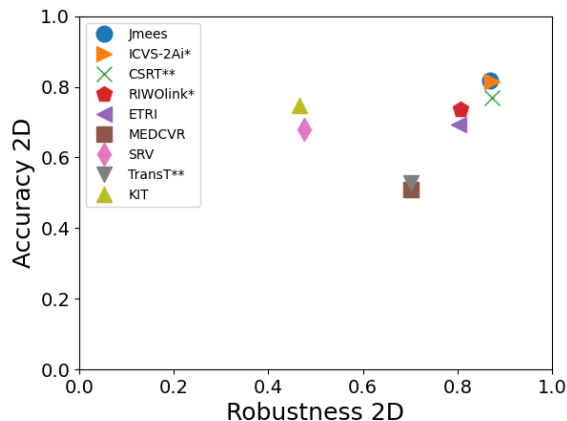


Figure 7: The accuracy-robustness plot on the test data. The better the performance, the closer to the top right corner.

dation, Visualization, Writing - Review & Editing, Project administration. **Samyakh Tukra:** Conceptualization, Data Curation, Writing - Original Draft. **Haozheng Xu:** Software, Writing - Original Draft. **Hiroki Matsuzaki:** Investigation, Writing - Original Draft. **Taiyo Ishikawa:** Investigation, Writing - Original Draft. **Minjun Kwon:** Investigation, Writing - Original Draft. **Yong Eun Jang:** Investigation, Writing - Original Draft. **Kwang-Ju Kim:** Investigation, Writing - Original Draft. **Gwang Lee:** Investigation, Writing - Original Draft. **Bizhe Bai:** Investigation, Writing - Original Draft. **Lueder Kahrs:** Investigation, Writing - Original Draft. **Lars Boecking:** Investigation, Writing - Original Draft. **Simeon Allmendinger:** Investigation, Writing - Original Draft. **Leopold Müller:** Investigation, Writing - Original Draft. **Yitong Zhang:** Investigation, Writing - Original Draft. **Yueming Jin:** Investigation, Writing - Original Draft. **Bano Sophia:** Investigation, Writing - Original Draft. **Francisco Vasconcelos:** Investigation, Writing - Original Draft. **Wolfgang Reiter:** Investigation, Writing - Original Draft. **Jonas Hajek:** Investigation, Writing - Original Draft. **Bruno Silva:** Investigation, Writing - Original Draft. **Lukas Buschle:** Investigation, Writing - Original Draft. **Estevão Lima:** Investigation, Writing - Original Draft. **João L. Vilaça:** Investigation, Writing - Original Draft. **Sandro Queirós:** Software, Investigation, Writing - Review & Editing. **Stamatia Giannarou:** Supervision.

## 9.2. Declaration of competing interest

The authors declare that they have no known competing financial interests or personal relationships that could have appeared to influence the work reported in this paper.

## Compliance with ethical standards

**Conflict of interest** The authors declare that they have no conflict of interest to disclose.

**Ethical approval** All human and animal studies have been approved and performed in accordance with ethical standards.

**Informed consent** All the data used for this publication was previously publicly available online and was obtained with informed consent.

**Funding** The authors are grateful for the sponsorship from Intuitive® and NVIDIA® for the prize awards.

## 10. Acknowledgments

The authors are grateful for the support from Intuitive® and NVIDIA® for sponsoring the prize awards. The authors are also grateful for the following research programs and grants: UK Research and Innovation (UKRI) Centre for Doctoral Training in AI for Healthcare (EP/S023283/1), the Royal Society (URF\R\201014),

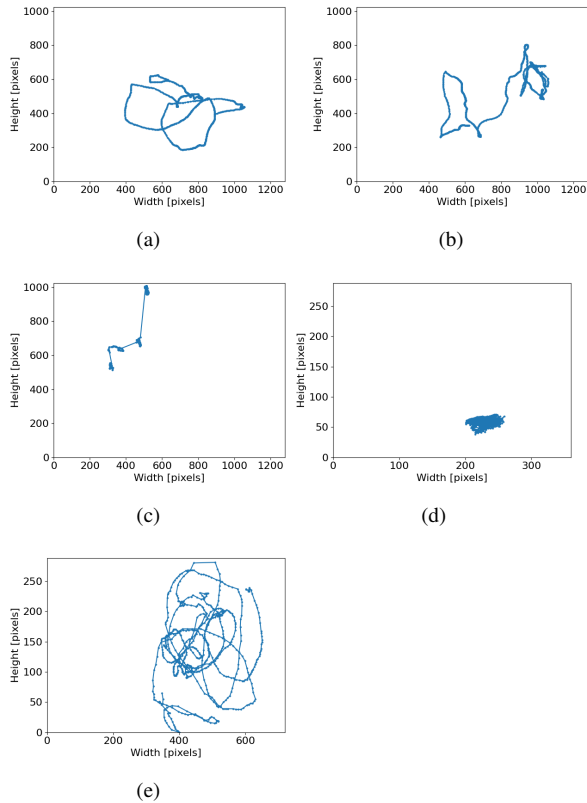


Figure 8: The motion of the left bounding box’s centre for video 1 of: (a) case 1, (b) case 2, (c) case 3, (d) case 4, and (e) case 5. In (e), the bounding box’s motion is spread out over the image plane, possibly creating a more difficult tracking task.

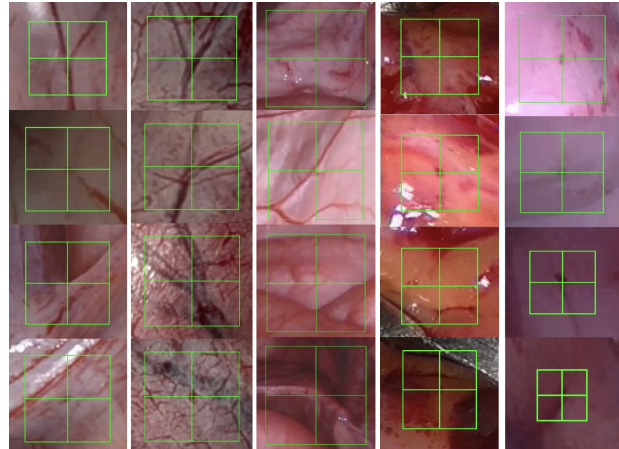


Figure 9: Bounding box samples from the hidden test subset. Each column corresponds to a case, from 1 (on the left) to 5 (on the right). It can be seen from cases 1, 2, 3 and 4 that the surface in and around the bounding box contains rich texture information. Conversely, the textures in case 5 are more homogeneous, lacking easy-to-identify features.

the Portuguese Foundation for Science and Technology (FCT; UIDB/50026/2020, UIDP/50026/2020, UIDB/05549/2020, UIDP/05549/2020, UIDB/50026/2020 and UIDP/50026/2020, and CEECIND/03064/2018), the Northern Portugal Regional Operational Programme (NORTE2020, under the Portugal 2020 Partnership Agreement, through the European Regional Development Fund; NORTE-01-0145-FEDER-000045 and NORTE-01-0145-FEDER-000059), the company KARL STORZ SE & Co. KG.

## References

- Allan, M., McLeod, A.J., Wang, C.C., Rosenthal, J., Hu, Z., Gard, N., Eisert, P., Fu, K.X., Zeffiro, T., Xia, W., Zhu, Z., Luo, H., Jia, F., Zhang, X., Li, X., Sharan, L., Kurmann, T., Schmid, S., Sznitman, R., Psychogyios, D., Azizian, M., Stoyanov, D., Maier-Hein, L., Speidel, S., 2021. Stereo correspondence and reconstruction of endoscopic data challenge. CoRR abs/2101.01133. URL: <https://arxiv.org/abs/2101.01133>, arXiv:2101.01133.
- Allan, M., Shvets, A., Kurmann, T., Zhang, Z., Duggal, R., Su, Y.H., Rieke, N., Laina, I., Kalavakonda, N., Bo-



- denstedt, S., et al., 2019. 2017 robotic instrument segmentation challenge. arXiv preprint arXiv:1902.06426 .
- Andrychowicz, M., Wolski, F., Ray, A., Schneider, J., Fong, R., Welinder, P., McGrew, B., Tobin, J., Pieter Abbeel, O., Zaremba, W., 2017. Hindsight experience replay. *Advances in neural information processing systems* 30.
- Bodenstedt, S., Speidel, S., Wagner, M., Chen, J., Kisilenko, A., Müller, B., Maier-Hein, L., Oliveira, B., Hong, S., Zamora-Anaya, J., et al., 2021. Heichole surgical workflow analysis and full scene segmentation (heisurf), MICCAI.
- Cartucho, J., 2022. Surgt’s ground truth labelling tool. URL: [https://github.com/Cartucho/SurgT\\_labelling](https://github.com/Cartucho/SurgT_labelling).
- Chen, X., Yan, B., Zhu, J., Wang, D., Yang, X., Lu, H., 2021. Transformer tracking, in: *Proceedings of the IEEE/CVF Conference on Computer Vision and Pattern Recognition*, pp. 8126–8135.
- Collins, T., Pizarro, D., Gasparini, S., Bourdel, N., Chauvet, P., Canis, M., Calvet, L., Bartoli, A., 2020. Augmented reality guided laparoscopic surgery of the uterus. *IEEE Transactions on Medical Imaging* 40, 371–380.
- Deng, J., Dong, W., Socher, R., Li, L.J., Li, K., Fei-Fei, L., 2009. Imagenet: A large-scale hierarchical image database, in: *2009 IEEE conference on computer vision and pattern recognition*, Ieee. pp. 248–255.
- Dosovitskiy, A., Beyer, L., Kolesnikov, A., Weissenborn, D., Zhai, X., Unterthiner, T., Dehghani, M., Minderer, M., Heigold, G., Gelly, S., et al., 2020. An image is worth 16x16 words: Transformers for image recognition at scale. arXiv preprint arXiv:2010.11929 .
- Garg, R., Roussos, A., Agapito, L., 2013. Dense variational reconstruction of non-rigid surfaces from monocular video, in: *Proceedings of the IEEE Conference on computer vision and pattern recognition*, pp. 1272–1279.
- Giannarou, S., Visentini-Scarzanella, M., Yang, G.Z., 2012. Probabilistic tracking of affine-invariant anisotropic regions. *IEEE Trans. Pattern Anal. Machine Intell.*
- Giannarou, S., Ye, M., Gras, G., Leibrandt, K., Marcus, H.J., Yang, G.Z., 2016. Vision-based deformation recovery for intraoperative force estimation of tool-tissue interaction for neurosurgery. *International Journal of Computer Assisted Radiology and Surgery* 11, 929–936. doi:10.1007/s11548-016-1361-z.
- Hattab, G., Arnold, M., Strenger, L., Allan, M., Arsentjeva, D., Gold, O., Simpfendorfer, T., Maier-Hein, L., Speidel, S., 2020. Kidney edge detection in laparoscopic image data for computer-assisted surgery. *Int. J. Comput. Assist. Radiol. Surg.* 15, 379–387. URL: <https://doi.org/10.1007/s11548-019-02102-0>, doi:10.1007/s11548-019-02102-0.
- He, K., Chen, X., Xie, S., Li, Y., Dollár, P., Girshick, R., 2022. Masked autoencoders are scalable vision learners, in: *Proceedings of the IEEE/CVF Conference on Computer Vision and Pattern Recognition*, pp. 16000–16009.
- Kalal, Z., Mikolajczyk, K., Matas, J., 2010. Forward-backward error: Automatic detection of tracking failures, in: *2010 20th International Conference on Pattern Recognition*, pp. 2756–2759. doi:10.1109/ICPR.2010.675.
- Kristan, M., Leonardis, A., Matas, J., Felsberg, M., Pflugfelder, R., Kämäräinen, J.K., Danelljan, M., Zajc, L.Č., Lukežič, A., Drbohlav, O., et al., 2020. The eighth visual object tracking vot2020 challenge results, in: *Computer Vision–ECCV 2020 Workshops: Glasgow, UK, August 23–28, 2020, Proceedings, Part V 16*, Springer. pp. 547–601.
- Kristan, M., Matas, J., Leonardis, A., Felsberg, M., Pflugfelder, R., Kämäräinen, J.K., Chang, H.J., Danelljan, M., Cehovin, L., Lukežič, A., et al., 2021. The ninth visual object tracking vot2021 challenge results, in: *Proceedings of the IEEE/CVF International Conference on Computer Vision*, pp. 2711–2738.

- Kristan, M., Matas, J., Leonardis, A., Vojir, T., Pflugfelder, R., Fernandez, G., Nebhay, G., Porikli, F., Čehovin, L., 2016. A novel performance evaluation methodology for single-target trackers. *IEEE Transactions on Pattern Analysis and Machine Intelligence* 38, 2137–2155. doi:10.1109/TPAMI.2016.2516982.
- Liu, L., Zhang, J., He, R., Liu, Y., Wang, Y., Tai, Y., Luo, D., Wang, C., Li, J., Huang, F., 2020. Learning by analogy: Reliable supervision from transformations for unsupervised optical flow estimation, in: *Proceedings of the IEEE/CVF Conference on Computer Vision and Pattern Recognition*, pp. 6489–6498.
- Lukežič, A., Vojří, T., Zajc, L.Č., Matas, J., Kristan, M., 2018. Discriminative correlation filter tracker with channel and spatial reliability. *International Journal of Computer Vision* 126, 671–688. URL: <https://doi.org/10.1007/s11263-017-1061-3>, doi:10.1007/s11263-017-1061-3.
- Lukežic, A., Vojir, T., Čehovin Zajc, L., Matas, J., Kristan, M., 2017. Discriminative correlation filter with channel and spatial reliability, in: *Proceedings of the IEEE conference on computer vision and pattern recognition*, pp. 6309–6318.
- Maier-Hein, L., Mersmann, S., Kondermann, D., Bordenstedt, S., Sanchez, A., Stock, C., Kenngott, H.G., Eisenmann, M., Speidel, S., 2014. Can masses of non-experts train highly accurate image classifiers?, in: *International conference on medical image computing and computer-assisted intervention*, Springer. pp. 438–445.
- Mountney, P., Stoyanov, D., Yang, G.Z., 2010. Three-dimensional tissue deformation recovery and tracking. *IEEE Signal Processing Magazine* 27, 14–24.
- Nicolau, S., Soler, L., Mutter, D., Marescaux, J., 2011. Augmented reality in laparoscopic surgical oncology. *Surgical oncology* 20 3, 189–201.
- Ozyoruk, K.B., Gokceler, G.I., Bobrow, T.L., Coskun, G., Incetan, K., Almalioglu, Y., Mahmood, F., Curto, E., Perdigoto, L., Oliveira, M., et al., 2021. Endoslam dataset and an unsupervised monocular visual odometry and depth estimation approach for endoscopic videos. *Medical image analysis* 71, 102058.
- Patel, H.A., Thakore, D.G., 2013. Moving object tracking using kalman filter. *International Journal of Computer Science and Mobile Computing* 2, 326–332.
- Pathak, D., Krahenbuhl, P., Donahue, J., Darrell, T., Efros, A.A., 2016. Context encoders: Feature learning by inpainting, in: *Proceedings of the IEEE conference on computer vision and pattern recognition*, pp. 2536–2544.
- Stoyanov, D., Mylonas, G.P., Deligianni, F., Darzi, A., Yang, G.Z., 2005. Soft-tissue motion tracking and structure estimation for robotic assisted mis procedures, in: *MICCAI* (2), pp. 139–146.
- Sun, D., Yang, X., Liu, M.Y., Kautz, J., 2018. Pwc-net: Cnns for optical flow using pyramid, warping, and cost volume, in: *Proceedings of the IEEE conference on computer vision and pattern recognition*, pp. 8934–8943.
- Twinanda, A.P., Shehata, S., Mutter, D., Marescaux, J., de Mathelin, M., Padoy, N., 2017. EndoNet: A Deep Architecture for Recognition Tasks on Laparoscopic Videos. *IEEE Transactions on Medical Imaging* 36, 86–97. URL: <http://ieeexplore.ieee.org/document/7519080/>, doi:10.1109/TMI.2016.2593957.
- Vaswani, A., Shazeer, N., Parmar, N., Uszkoreit, J., Jones, L., Gomez, A.N., Kaiser, Ł., Polosukhin, I., 2017. Attention is all you need. *Advances in neural information processing systems* 30.
- Wang, C., Cartucho, J., Elson, D., Darzi, A., Gianarou, S., 2022. Towards autonomous control of surgical instruments using adaptive-fusion tracking and robot self-calibration, in: *2022 IEEE/RSJ International Conference on Intelligent Robots and Systems (IROS)*, IEEE. pp. 2395–2401.
- Wang, N., Song, Y., Ma, C., Zhou, W., Liu, W., Li, H., 2019. Unsupervised deep tracking, in: *The IEEE Conference on Computer Vision and Pattern Recognition (CVPR)*.
- Wang, N., Zhou, W., Song, Y., Ma, C., Liu, W., Li, H., 2021. Unsupervised deep representation learning for

- real-time tracking. *International Journal of Computer Vision* 129, 400–418.
- Wang, Z., Li, X., Navarro-Alarcon, D., Liu, Y.h., 2018. A unified controller for region-reaching and deforming of soft objects, in: 2018 IEEE/RSJ International Conference on Intelligent Robots and Systems (IROS), IEEE. pp. 472–478.
- Weld, A., Cartucho, J., Xu, C., Davids, J., Giannarou, S., 2022. Regularising disparity estimation via multi task learning with structured light reconstruction. *Computer Methods in Biomechanics and Biomedical Engineering: Imaging & Visualization* .
- Ye, M., Johns, E., Handa, A., Zhang, L., Pratt, P., Yang, G.Z., 2017. Self-supervised siamese learning on stereo image pairs for depth estimation in robotic surgery. *arXiv preprint arXiv:1705.08260* .
- Zhan, J., Cartucho, J., Giannarou, S., 2020. Autonomous tissue scanning under free-form motion for intraoperative tissue characterisation, in: 2020 IEEE international conference on robotics and automation (ICRA), IEEE. pp. 11147–11154.